



3D effects of sharp boundaries at the borders of the African and Pacific Superplumes: Observation and modeling

Akiko To^{a,*}, Barbara Romanowicz^a, Yann Capdeville^b, Nozomu Takeuchi^c

^a*Seismological Laboratory, University of California, Berkeley, 215 MCone Hall, Berkeley, CA 94720, USA*

^b*Institut de Physique du globe de Paris, 4, place jussieu, Paris, 75005, France*

^c*Earthquake Research Institute, University of Tokyo 1-1-1, Yayoi, Bunkyo-ku, Tokyo 113-0032, Japan*

Received 13 September 2004; received in revised form 6 January 2005; accepted 18 January 2005

Available online 24 March 2005

Editor: Scott King

Abstract

We report that a sharp lateral boundary exists at the southern edge of the Pacific superplume. The set of SHdiff waveforms, which graze the South Pacific, have similar features to those observed previously at the southeastern edge of the African superplume. Both waveform sets show a rapid shift of the arrival time and the broadening of the waveforms with respect to the azimuth as previously reported in the case of the African plume. We also document here that they both show a secondary pulse that follows the direct Sdiff phase. The coupled mode/spectral element method, which can handle strong lateral variations of shear velocity in D'' , is used to construct synthetic waveforms. The postcursors can be explained by simple effects of 3D structure in the D'' region with a sharp quasi vertical boundary aligned almost parallel to the ray path. The existence of these pulses suggests that modeling of heterogeneity outside of the great circle path can help constrain the 3D structure at the base of the mantle. When including 3D effects in the modeling, we find that the velocity contrast across the sharp boundary is of the order of 4–5%, averaged over the last 300 km of the mantle, which is smaller than has been proposed in some studies, but larger than in existing tomographic models, implying that the “superplume” features at the base of the mantle cannot be purely thermal. The similarity of the two observed SHdiff waveform sets at relatively high frequencies indicates that the low velocity regions in the lower mantle under Pacific and Africa, corresponding to the strong degree-2 pattern in shear velocity tomographic models, have a similar nature also at finer scales.

© 2005 Elsevier B.V. All rights reserved.

Keywords: D'' region; Low velocity structure; Sdiff; Super plume

1. Introduction

Global shear velocity tomographic models show two large scale low velocity structures in the lower mantle, one under southern Africa and the other under

* Corresponding author. Tel.: +1 510 642 3977.

E-mail address: toh@seimo.berkeley.edu (A. To).

the mid-Pacific [1–5]. The long wavelength structures of the so-called superplumes are consistent between different models and they extend laterally for several thousand kilometers. However, disagreement remains in the finer scale structures, which are better resolved by forward modeling techniques. More detailed images of the strength and shape of the slow anomalies are often obtained by matching the travel time data and waveforms of various lower mantle sensitive phases such as ScS, S, SpdKS, SKKS, SKS and Sdiff [6–11].

Recently, sharp lateral transitions in the velocity structure at the borders of the superplumes have been reported. Most of the findings are associated with the African superplume [12,13]. Steep gradients of the shear wave velocity are observed on the east and west sides of this prominent low velocity feature, which extends 1500 km above the CMB [13]. Furthermore, on the southeastern edge of the African anomaly, sharp transitions are observed at the north and south sides of the kidney shaped slow anomaly (shown as a brown dashed line in Fig. 1) that lies on the CMB [12,15].

There is also evidence of sharp velocity gradients around the Pacific superplume. A large 8% lateral shear velocity drop in D'' has been observed in the northeastern Pacific with a localized region of fast anomaly adjacent to the edge of the superplume [16].

The two prominent low S velocity features in the Pacific and under Africa have been interpreted as large scale upwellings, with higher than average temperature, possibly representing the return flow from subduction [17]. The low velocities are anti-correlated with bulk sound speed [18,19], and may be associated with higher than average density [20]. Their detailed features are not resolved yet, in particular whether the corresponding upwellings are broad or consist of a large number of narrow plumes [21]. The sharp velocity contrasts documented in some previous studies [5,12,13,15,16] also indicate that the nature of the superplumes cannot be purely thermal. Constraining the gradients across their boundaries and the detailed structure within them is therefore crucial to furthering our understanding of the dynamics of the mantle.

We focus on two points in this paper. First, we show that a sharp vertical boundary also exists at the southern edge of the Pacific superplume. The set of SHdiff waveforms, which sample D'' in the South Pacific, have similar features to those observed at the southeastern edge of the African superplume [12,15]. Second, we show that the waveforms from Africa and the South Pacific exhibit not only rapid travel time shifts, but also multiple pulses, for paths sub-parallel to the sharp boundary, in its vicinity. We use the coupled mode/spectral element method (CSEM in what follows) [22–24] to construct synthetic wave-

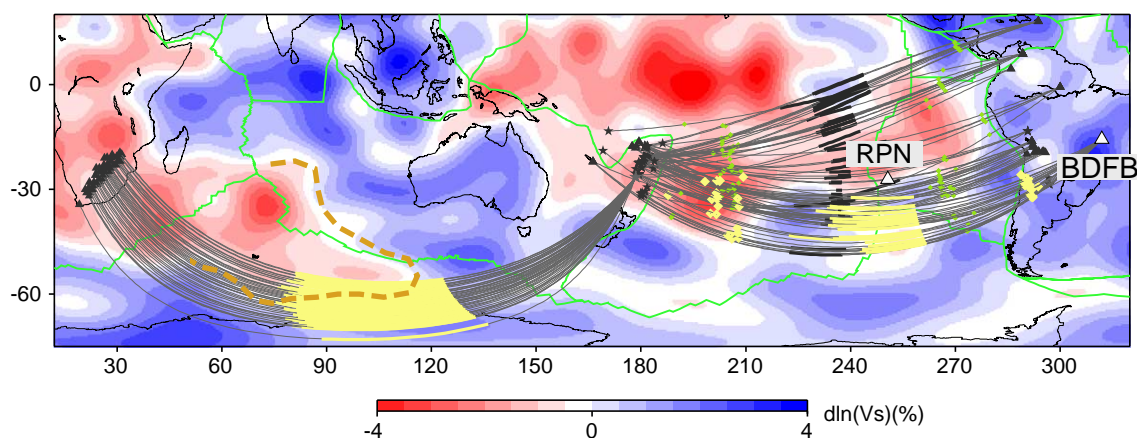


Fig. 1. Earthquakes (stars), stations (triangles), and projections of the raypaths. Background model is the shear velocity model SAW24b16 [3] at the depth of 2850 km. The thick lines show the diffracting portion of the paths on the CMB. Thick yellow lines are the paths of the traces whose waveforms are shown in Figs. 2 and 3. Diamonds show the points where SKKS enter and exit the outer core.

forms in 3D models of D'' and show that these first order features and their trends with azimuth can indeed be produced by 3D effects from a simple structure with a strong sharp quasi vertical boundary aligned almost parallel to the ray path.

2. Data

The locations of the events and stations used are displayed in Fig. 1. We considered earthquakes with depths of 100–680 km and $M_w \geq 6.1$. Broad-band seismograms were collected from the IRIS/GSN and IRIS/PASSCAL networks. Fig. 2 shows the observed Sdiff waveforms for an event in the Fiji–Tonga region (19970904) recorded at the stations of the Tanzanian array in Africa. The locations of raypaths are shown in Fig. 1. Waveforms are aligned with respect to the Sdiff arrival time predicted for PREM [14] and shown in order of increasing azimuth. As the azimuth increases, the ray paths start to enter the slow anomaly that lies to the north (Fig. 1). The first two panels from the left show transverse and radial components respectively, to which a zero-phase butterworth filter has been applied, with corner frequencies of 0.01 and 0.2 Hz. A bandpass filter with slightly different high corner frequencies is applied to the traces of the third and fourth panel, to match the filters used later in the synthetic computations. The high frequency corners are at 0.09 and 0.078 Hz respectively.

Fig. 3 shows the SHdiff records of Fiji and Tonga events recorded at station BDFB of the Global Telemetered Southern Hemisphere Network (GTSN), in Brazil. The source information for each event is given in Table 1. The SH radiation patterns for the Harvard CMT solution (<http://www.seismology.harvard.edu/CMTsearch.html>) are shown in Fig. 4. The waveforms are corrected for source polarity according to the latter solution. The raypaths of these waveforms are shown in thick yellow lines in Fig. 1: they sample the southern Pacific. The configuration of the events and stations is different from that of the African case (Fig. 2) in that we look at waveforms from many events recorded at a single station, whereas waveforms from one event, recorded at many stations, are aligned in the African case. This is because there is at

present no dense array in South America that would sample this region. Consequently, the waveforms of Fig. 3 are shown in order of back azimuth. The waveforms look alike, despite the fact that we are comparing waveforms from earthquakes with different sizes, depths and mechanisms, and with possible shifts due to errors in the event location and timing. A clear time delay of about 13 s of the top trace, which samples the north, compared to the bottom trace, which samples the south, is observed. The S phase waveforms recorded at the closer station RPN, at distances of 61–64° (Fig. 1) show relatively simple pulses (Fig. 5) and do not show either secondary pulses or the rapid time shift with respect to the back azimuth. The waveforms, especially from the event 20000614, show the distinct difference between a simple S phase and a complex SHdiff phase. These comparisons confirm that the travel time shift and the secondary pulses in the SHdiff phase reflect an anomalous structure and are not due to features in the source process. There is no systematic trend in the radiation pattern (Fig. 4) and the size and depth of the earthquakes (Table 1) with respect to the back azimuth, which also indicates that the features of the Sdiff phase are not due to the source processes or to structure in the vicinity of the source.

These SHdiff waveform sets, which sample the southeastern edge of the African slow anomaly (hereafter ASA) and the southern edge of the Pacific slow anomaly (hereafter PSA), are very similar in the following ways. First of all, the onset times of the first arrivals change very rapidly, or show a sudden jump with respect to the change of azimuth or back azimuth. The thick grey lines in Figs. 2 and 3 follow the trough of the first arrival. In the case of ASA, the first arrivals shift about 15 s within an 18° change of azimuth. In the PSA case, the arrival time changes about 13 s within the 18° change in back azimuth. Second, the waveforms, which graze the transition from fast to slow, show an additional pulse indicated by solid dots and solid black lines in Figs. 2 and 3. In the ASA case, as raypaths start to sample the slow anomaly, this pulse comes closer to the first pulse, and it finally merges with the latter at an azimuth of 218°. In other words, the solid black lines, which follow the second pulse, have the opposite slope from the grey lines that follow the first pulse (in the right 2 panels of Figs. 2 and 3).

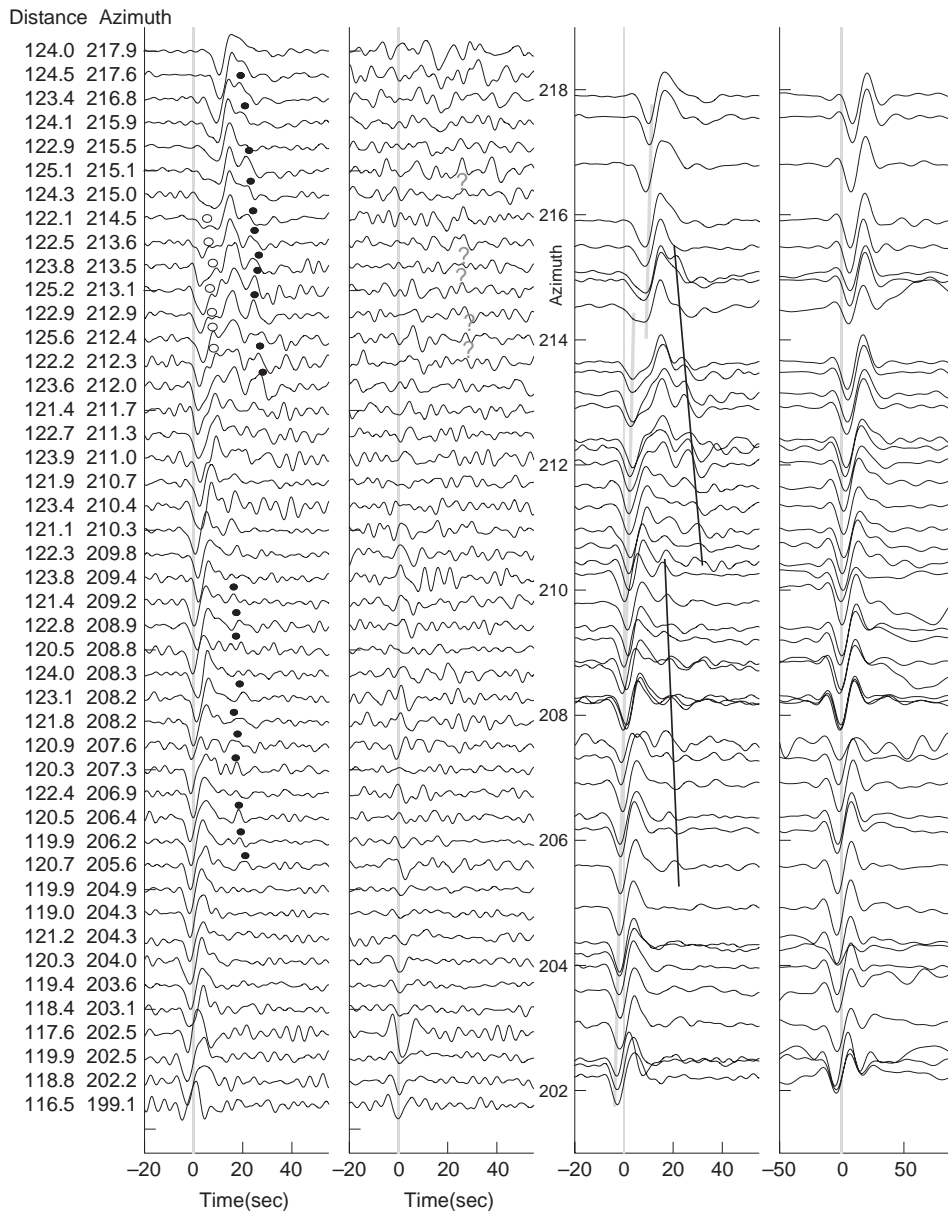


Fig. 2. Observed velocity waveforms for event 19970904 in Fiji–Tonga (M_w 6.8) recorded in South Africa. Waveforms are filtered in three different ways. First panel from the left: Transverse component bandpass filtered with corner frequencies at 0.01 and 0.5 Hz. The distance and back azimuth of each station are indicated on the left. The broken line is the expected Sdiff arrival for the PREM model. Second panel: Radial component, filtered in the same way as the transverse component. Third panel: Bandpass filtered with corner frequencies at 0.01 and 0.125 Hz. Y-axis shows the back azimuth. Note the different vertical scale compared to the first two panels on the left. Right panel: filtered in the same way as synthetic waveforms in Fig. 8, with a high end corner frequency at 0.078 Hz. With this frequency limit, the multiple pulses are not well separated. Gray lines follow the trough of the first pulse. Black solid lines follow the secondary pulse, which is only observed in the vicinity of the structural boundary.

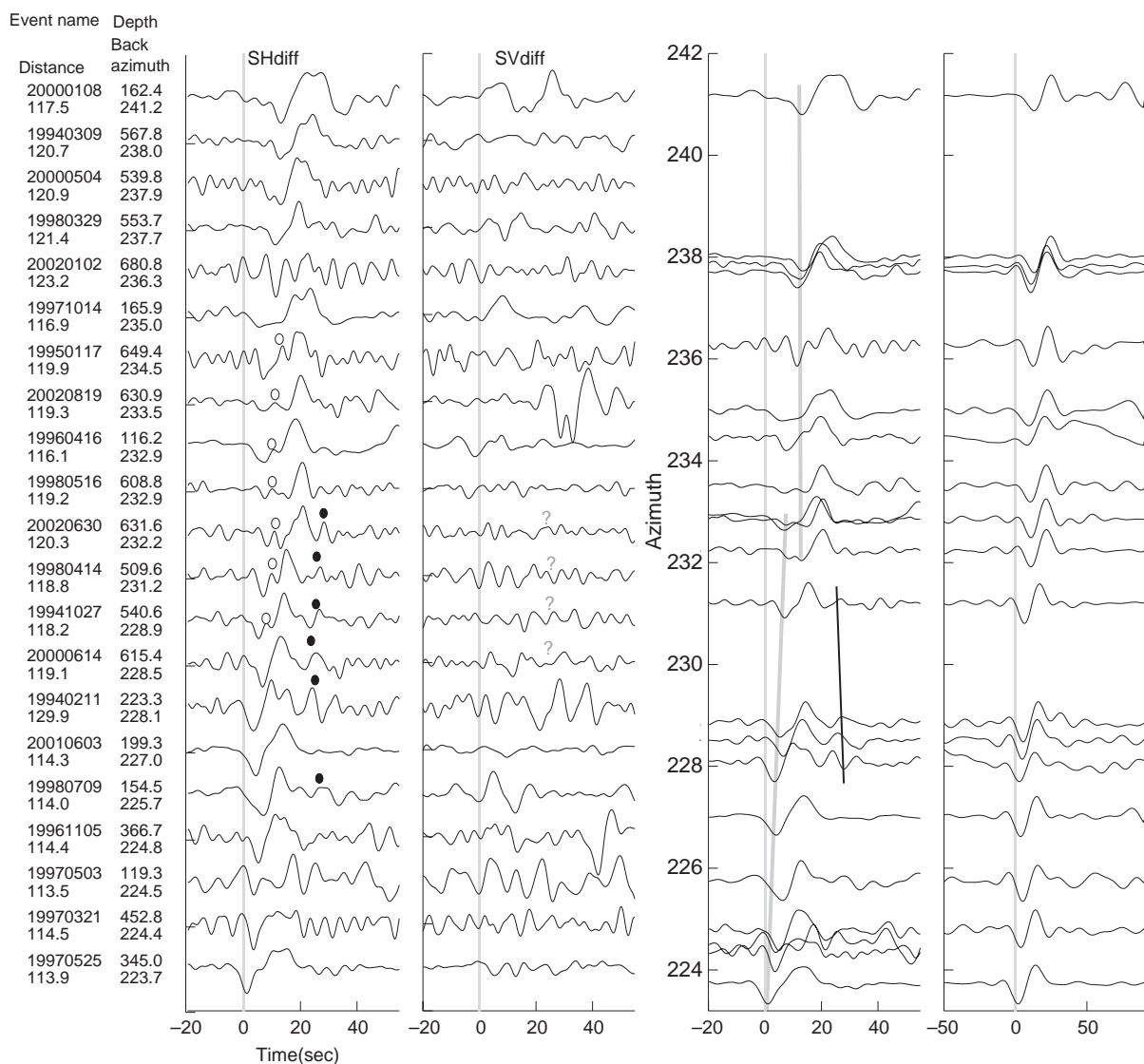


Fig. 3. Same as Fig. 2 for 21 events in Fiji-Tonga recorded at station BDFB in Brazil, ordered as a function of back azimuth. Filtered in the same way as Fig. 2. The large pulse in the radial component of event 20020819 is a contamination from an event which occurred 7 min later.

This later phase is the feature we model in the following section. Third, when we look at the higher frequency components of these waveforms, there are yet additional pulses that can be followed for a certain azimuth range. These pulses are shown by the open circle dots in the first panel of Figs. 2 and 3.

In order to confirm that the travel time shift observed in PSA is due to heterogeneity at the base of the mantle, we measured the differential travel times of Sdiff–

SKKS (Fig. 6). We measured them for all the paths shown on the Pacific side in Fig. 1. The differential travel times are less affected by the uncertainty in the source location and the origin time than for absolute Sdiff. In addition, because the raypaths of Sdiff and SKKS are close to each other in the upper mantle, they are more sensitive to heterogeneity at the base of the mantle. Both Sdiff and SKKS travel times are measured by taking cross correlations between observed wave-

Table 1
List of events used in this study and recorded at station BDFB in Brazil

Event date	Latitude	Longitude	Depth (km)	Distance (°)	Back azimuth (°)	Mw	Half duration (s)
1997 05 25	−32.02	−179.95	345.0	113.84	223.7	7.1	8.5
1997 03 21	−31.18	179.90	452.8	114.46	224.37	6.3	3.5
1997 05 03	−31.70	−179.06	119.3	113.5	224.5	6.9	7.0
1996 11 05	−30.95	−179.73	366.7	114.4	224.8	6.7	5.8
1998 07 09	−30.51	−178.71	154.5	114.0	225.7	6.9	6.8
2001 06 03	−29.37	−178.23	199.3	114.3	227.0	7.1	9.3
1994 02 11	−18.89	169.08	223.3	129.9	228.1	6.8	6.5
2000 06 14	−25.45	178.38	615.4	119.02	228.52	6.4	4.1
1994 10 27	−25.75	179.39	540.6	118.11	228.87	6.6	5.2
1998 04 14	−23.73	−179.81	509.6	118.69	231.21	6.1	2.7
2002 06 30	−22.13	179.43	631.6	120.18	232.25	6.4	4.0
1996 04 16	−23.98	−176.47	116.2	116.1	232.9	7.1	9.3
1998 05 16	−22.27	−179.35	608.8	119.17	232.85	6.8	6.5
2002 08 19	−21.74	−179.08	630.9	119.26	233.51	7.6	16.5
1995 01 17	−20.71	−179.13	649.4	119.86	234.47	6.3	3.0
1997 10 14	−21.94	−176.15	165.9	116.9	235.0	7.7	17.9
2002 01 02	−17.63	178.84	680.8	123.15	236.26	6.1	3.0
1998 03 29	−17.57	−178.85	553.7	121.31	237.70	7.1	9.3
2000 05 04	−17.72	−178.31	539.8	120.80	237.87	6.4	4.2
1994 03 09	−17.69	−178.11	567.8	120.65	238.01	7.6	16.0
2000 01 08	−16.84	−173.81	162.4	117.5	241.2	7.2	9.7

The waveforms for these events are shown in Fig. 3. The origin times and locations are extracted from the Harvard CMT Catalog.

forms and PREM synthetic waveforms constructed by normal mode summation down to 5 s.

A bandpass filter with corner frequencies of 0.01 and 0.058 Hz is applied to the Sdiff phase and a filter with corner frequencies of 0.01 and 0.2 Hz is applied to the SKKS phase to measure the travel times. Relatively low frequency components are used for the Sdiff measurement because the Sdiff waveforms look complex, with many high frequency pulses, as shown in the first and third panels of Fig. 3. Taking the cross correlation is difficult in such cases and results in the reduction of the number of usable data. High frequency components are used for the SKKS measurements to avoid contamination by other phases such as SKKKS, which arrives close to SKKS. When measured using different frequency ranges, including down to 0.2 Hz for Sdiff and 0.058 Hz for the SKS, the measured travel times shift globally by a few seconds. However the relative travel time differences between the stations, which are the focus here, change by less than 1.5 s.

The result of the travel time measurement is shown in Fig. 6 with respect to the latitude of the point where

Sdiff first reaches the CMB on the source side. An ellipticity correction [26] is applied to each datum. The residuals of Sdiff–SKKS for the station BDFB (gray diamonds in Fig. 6) show a steep gradient of 10 s within a latitude change of 10°. This indicates that the rapid shift of the arrival time shown in Fig. 3 is neither due to the mislocation of events nor to upper mantle heterogeneity. This shows that the sharp lateral transition in shear velocity anomaly lies between the two regions where the SKKS raypaths enter and exit the outer core (shown by yellow diamonds in Fig. 1). The data points for stations other than BDFB also show that the Sdiff–SKKS residuals increase toward the north up through a latitude of around −20°. The residuals decrease again north of latitude of −15°, suggesting a rapid exit from the low velocity region, but this feature is not discussed further in this paper.

3. Modeling from simple structures

We used a coupled mode and spectral element approach (CSEM in what follows) [22–24] for the

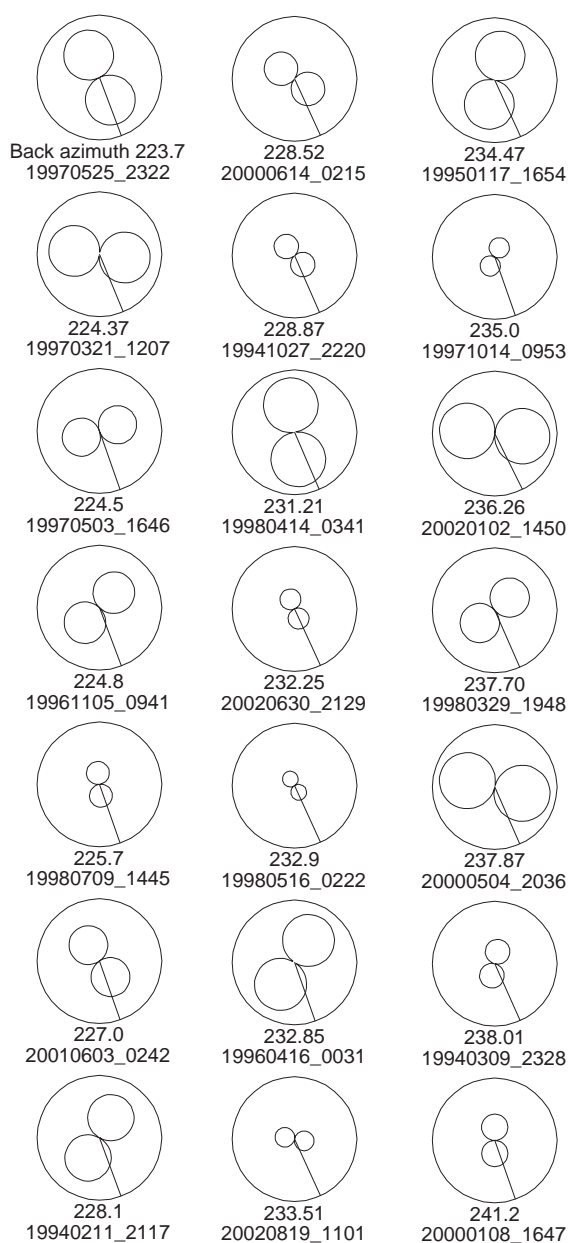


Fig. 4. SH wave radiation pattern of the Fiji–Tonga events recorded at station BDFB. The radiation patterns are evaluated in the great circle plane, which connects the source and receiver. The straight line in each plot shows the take-off angles of Sdiff phase. The mechanisms are from the Harvard CMT Catalog. (<http://www.seismology.harvard.edu/CMTsearch.html>). They are shown in order of back azimuth from BDFB from the top left to bottom right.

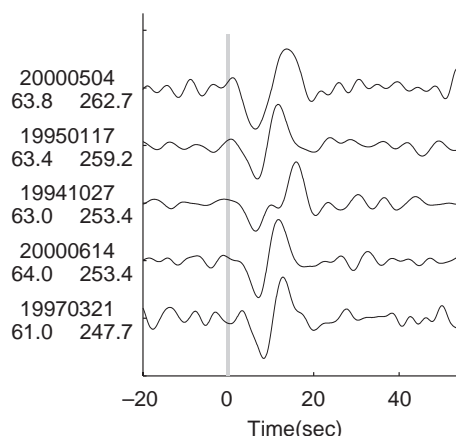


Fig. 5. S waveforms for those events listed in Table 1, recorded at station RPN (shown in Fig. 1), for which data are available. The event date, epicentral distance (left) and azimuth (right) are indicated on the left of the traces. The simple S phase waveforms indicate that the secondary pulses in the SHdiff waveforms in Fig. 3 are due to heterogeneous structure rather than to the source process. Event 19941027 has a secondary pulse around 10 s after the first motion, but this cannot be related to that observed for SHdiff, as the latter arrives much later, about 25 s after the first motion.

waveform modeling. The study of strong lateral variations in the D'' region is best addressed by a forward waveform modeling approach that can handle 1) the propagation of seismic waves in 3D models with strong lateral variations and in spherical geometry and 2) diffracted waves along the core–mantle boundary. The most promising method at the present time, the spectral element method (SEM), remains computationally heavy. To address the study of heterogeneity in particular regions, such as D'' , Capdeville [22] developed a hybrid method that couples spectral element computations with a normal mode solution, so that the spectral element method is used only in the target strongly heterogeneous regions. The modal solution provides a fast and precise solution in regions of the Earth where a model with spherical symmetry can be considered. This approach has been extended to the case of a heterogeneous shell “sandwiched” between two spherically symmetric shells [24,25]. In this study, SEM is used for the bottom 370 km of the mantle.

In the first part, we show that synthetic waveforms constructed from simple models with vertical boundaries can explain the first order features of the observed waveforms. The models have the 1D structure of PREM down to a depth of 2591 km,

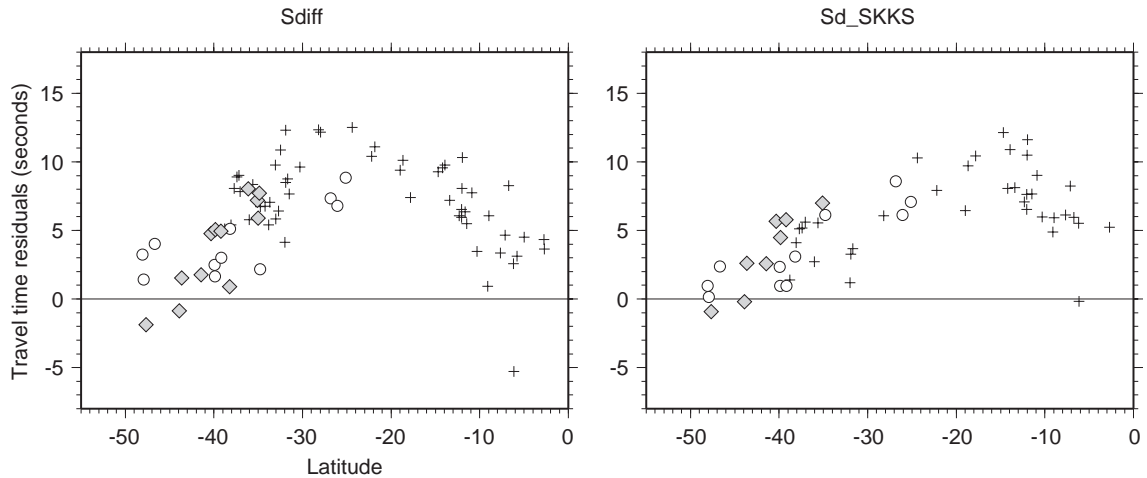


Fig. 6. Travel time shifts as a function of latitude of the point where the Sdiff raypath reaches the CMB. Left: absolute Sdiff travel time residual with respect to PREM. Right: differential travel time residuals of Sdiff-SKKS. Diamonds correspond to the data at station BDFB. Crosses are data for Fiji-Tonga events. Circles are data for South American events. Both Sdiff and Sdiff-SKKS show a steep gradient with respect to latitude.

and the 3D model below 2591 km, down to the CMB. The 3D part of Model 1 is divided into 4 quadrants as shown in Fig. 7a so that we can test different models with the same CSEM run. Each quadrant in Model 1 has either -3% or $+3\%$ constant S velocity anomaly with respect to PREM. The portion of the Sdiff raypaths, which goes through the bottom 300 km of the mantle, is shown in thick lines. The source mechanism is set to have its maximum SH radiation around the maximum gradient of lateral heterogeneity. The two boundaries on the right and top (i.e. pointing 0° N and 90° E) are sharp and the other two on the left and bottom (i.e. pointing 180° S and 90° W) are more gradual. The 6% velocity jump occurs within a distance of 3° for the sharp boundary and within 10° for the gradual boundary. The sharp boundaries are shifted 13° from the great circle that goes through the source (shown by a dashed line). The gradual boundaries lie between 5° and 15° from the great circles. Model 2 (Fig. 7b) has an S velocity anomaly of -2% and $+2\%$ in the fast and slow region, respectively. The 4% shear velocity jump occurs within 7° . The boundaries lie 13° away from the great circles, which are parallel to the boundaries.

Fig. 8(a–d) show the synthetic waveforms for the stations which are located at the four velocity transition zones of Model 1. The synthetics are computed down to 12 s. Each trace is normalized by

its maximum amplitude. Bars on the right side show the relative maximum amplitude. Long bars indicate that the traces have large maximum amplitudes. The four panels show different combinations according to whether the interface is sharp or gradual and whether the source is located on the slow or fast side of the interface. In all four cases, we observe multiple pulses for paths which interact with transitions in the velocity structure. The comparisons between (a) and (c), and between (b) and (d) show that a sharper boundary produces a multiple pulse in a wider range of azimuths. When the source is located in the slow region (Fig. 8 (a)(c)), the secondary pulse, indicated by dashed lines, is observed at stations in the slow regions, such as stations 23–41 for (a), 203–221 for (c). By inspecting the corresponding particle motions, we infer that this corresponds to paths which are radiated toward the fast region from the slow region, turn within the velocity gradient and propagate toward the stations in the slow region. The estimated bent raypath is shown in Fig. 7a for station 205 of Model 1. The path is estimated by setting the lateral turning point of the ray in the middle of the diffracting portion on the CMB. When the path from the source enters D'' in the fast region ((b), (d)), a secondary phase due to multipathing is observed, as indicated by the solid black lines in Fig. 8(b) and (d). It is observed at stations 81–105 for (b), 261–281 for (d). The first

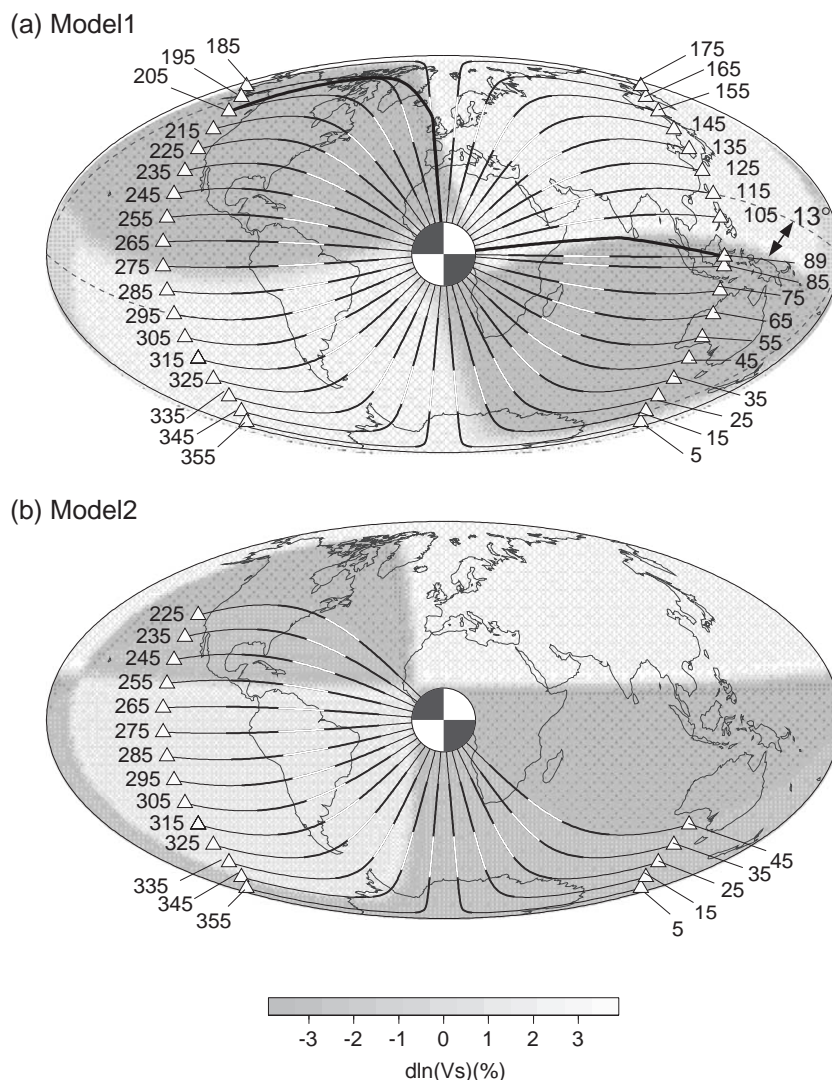
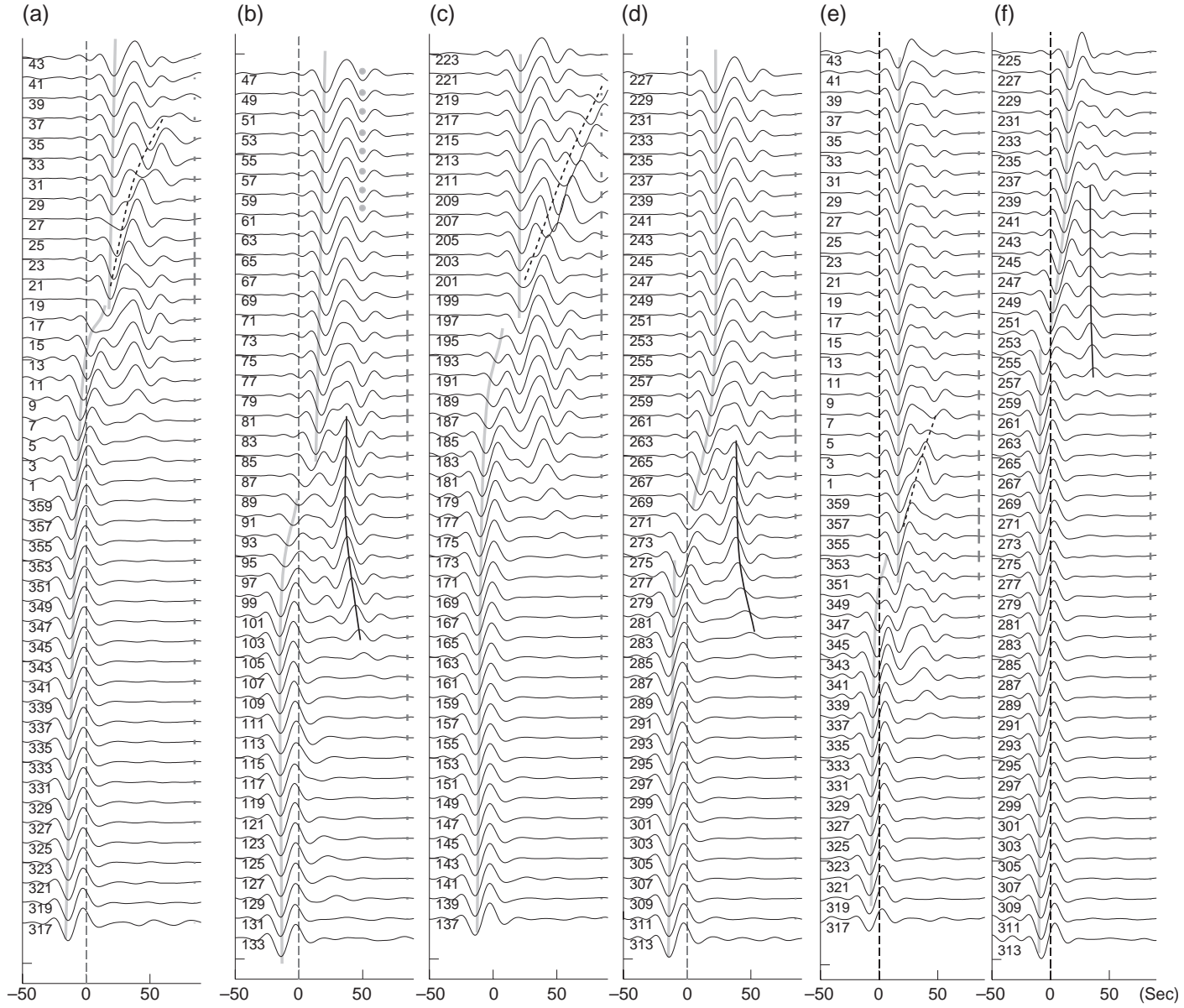


Fig. 7. The shear velocity models used in the CSEM synthetic waveform calculation. (a) Model 1: The fast and slow regions have velocity anomalies of -3% and $+3\%$ respectively with respect to PREM. The sharp boundaries are located in the top and right (North trending and East trending, thin white lines), and gradual boundaries are on the left and bottom. The sharp boundaries are shifted 13° away from the great circles, which are parallel to them (shown by a dashed line). The gradual boundaries are oriented between 5° and 13° from the great circles. (b) Model 2: The fast and slow regions have velocity anomalies of -2% and $+2\%$ respectively. The boundaries are shifted 15° away from the great circles which are parallel to the interface. Thick dark lines show the portion of Sdiff raypath, which samples the bottom 300 km of the mantle. Thick white lines show the diffracting portion at the CMB. The numbers next to the stations are azimuths measured from the south. They also serve as the station names in Fig. 8. Raypaths of 1D model are shown except for station 89 and 205 in Model 1 where multipathing are shown by thick black lines.

arrival at these stations is a wave which is refracted at the boundary from the fast to slow region. For example, the refracted raypath for station 89, estimated from the particle motion, is drawn in Fig. 7. The secondary phase at these stations is a wave which

propagates directly from the source without bending much, sampling the slow region in D'' . The move out of the phase indicated by the black line is observed at stations in the fast region or at the border, such as stations 101–105 and 277–281. We believe this is a



diffracted wave originating from the scattering point where the boundary of the fast and slow region meets the 1D PREM at 300 km above the CMB, and is therefore an unrealistic feature of the model. Fig. 8 (e) and (f) show the result for Model 2, which has a smaller shear velocity transition (from -2% to 2%). The source is located on the slower side in (e) and the faster side in (f). Explanation of the phases shown by solid black and dashed lines are the same as above.

Among the six panels in Fig. 8, the waveforms of panel (f) show features which resemble the observations most. The velocity contrast at the boundary is 4% and the source is located on the fast side of the boundary. A more direct comparison between the synthetic and observed waveforms is shown in Fig. 9. Although there are some differences, they all have the common feature of one trough followed by two peaks. The waveforms are compared with different time scales and frequency ranges, to show the qualitative similarity between them. The time scale of the synthetics is stretched compared to that of the observed waveforms. This is because of the frequency limitation of the present SEM calculations, which is dictated by the computer power available to us. Although synthetics were calculated down to 8 s in the next section, it is limited down to 12 s here due to the heavy computations. In the comparison shown in Fig. 9, we have chosen a station, which clearly shows two separate pulses in the synthetics. As the second pulse moves closer to the first one (229–231 of Model 2), these pulses blend into a single broadened pulse because frequency resolution is not good enough. Calculations of the CSEM synthetics to higher frequencies would allow a better separation of these pulses for paths close to the vertical boundary, as seen in the observations. The waveforms from Model 2

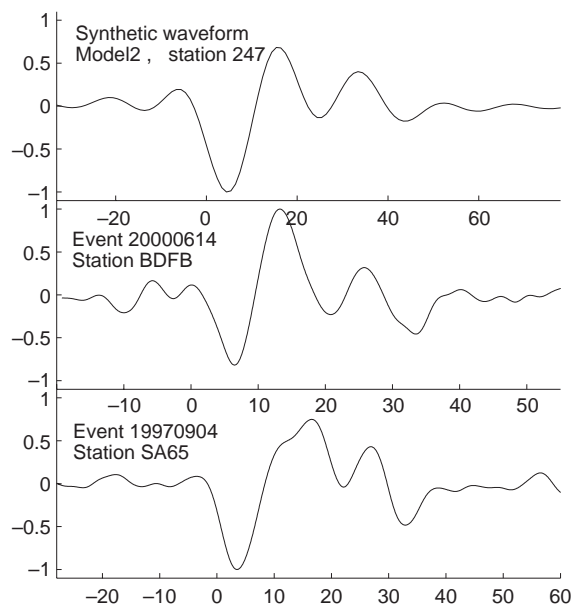


Fig. 9. Comparison between observed and synthetic waveforms. Top: CSEM synthetics as in Fig. 8. Middle: an observed waveform that samples PSA, band-pass filtered with corner frequencies at 0.01 and 0.125 Hz. Bottom: an observed waveform that samples ASA. In Fig. 2 (a) this trace is shown at a back azimuth of 212° , but bandpass filtered with corner frequencies at 0.01 and 0.10 Hz. The time scale of the synthetic is stretched compared to that of the observed waveforms. This is because among the synthetic waveforms, we have chosen a station which clearly shows the two crests separately. Stations that are closer to the boundary would present the two pulses closer to each other, however with the frequency limitation those pulses would blend into a single broadened pulse.

look more similar to the data than Model 1, which provides constraints on the appropriate velocity contrast to match the observations. As shown later, the velocity contrast which explains the Sdiff travel time measurements in the case of ASA is about 4% and it is consistent with Model 2. The first arrival of

Fig. 8. Synthetic waveforms calculated using CSEM for the models shown in Fig. 7. Each trace is normalized by its maximum amplitude. Bars on the right side show the relative maximum amplitude. The waveforms in the four panels (a)–(d) are calculated for Model 1 which has a 6% lateral shear velocity jump (-3% to $+3\%$). They show different combinations according to whether the interface is sharp (c)(d) or gradual (a)(b) and whether the source is located on the slow (a)(c) or fast (b)(d) side of the interface. The waveforms in the last two panels (e) and (f) are calculated for Model 2, which has a lateral velocity jump of 4% . The source is located in the slow region for (e), and in the fast region for (f). The gray lines follow the trough of the first pulse. When the source is located in the slow anomaly region ((a), (c) and (e)), large postcursors (dashed lines) are observed at the receivers located in the slow regions. They correspond to paths turning within the velocity gradient. They are observed at stations 24–41 for (a), 221–203 for (c) and 1–7 for (e). When the source is located in the fast region ((b), (d) and (f)), a secondary phase due to refraction and diffraction is observed as indicated by the black solid lines. They are observed at stations 81–105 for (b), 261–281 for (d) and 231–259 for (f). The waveforms which sample only the slow regions (stations at 47–63, 227–241 for Model 1, 13–41 for Model 2) show additional pulse which are indicated by grey dots. We think the pulses are due to the vertical velocity change in the synthetic model, which is the sudden reduction of velocity at 300 km above the CMB.

Model 2 at station 247 is a refracted wave from the fast region to the slow region (similar to station 89 in Model 1, Fig. 7a). In Model 1 however, the bending of the ray at the boundary is large and creates a large shadow zone of the first arrival, which does not seem to be present in the observations.

4. Modeling based on the tomographic model

In the second part of the modeling, we focus on the kidney shaped slow anomaly in Africa. As shown in the previous section, the cause of the multiple pulses depends on the geometry of the source and receiver, and the location of the boundary. Based on the SH tomographic model [3], we constructed a model which generates the secondary phase (solid black lines of Fig. 2). The result gives insight of where and how the secondary arrivals are produced in the African data. Fig. 10 presents equidistance projections of the kidney shaped anomaly. The source, in the Fiji–Tonga region, is plotted at the apex. The left panels show the original SAW24B16 model. The right panels show a modified model. The contour line of 0 (%) anomaly of the original tomographic model is kept fixed. The velocity anomaly is saturated to -2.75 (%) in the slow regions and 1.75 (%) in the fast region, between the CMB and 300 km above the CMB. These values are chosen to fit the travel time measurements of the Sdiff phase. The transition to the 1D model above 370 km from the CMB is here smooth, to avoid artificial effects in the vertical plane. Fig. 11 shows the synthetic waveforms calculated down to 8 s. The calculation to high frequencies is necessary because the secondary arrival cannot be distinguished for some paths when periods shorter than 12 s are not included, as shown in Fig. 2. The synthetics from the original tomographic model (Fig. 11 left panel) do not generate the secondary arrival or the rapid shift of the first arrival. On the other hand, the synthetics from the modified model with the sharp boundaries (Fig. 11 right panel) capture the features of the observed waveforms. The move out of the secondary arrival, which actually appears in multiple branches, shows a slope which is consistent with observations, although it appears at a slightly different azimuth. Moreover, the jump of the first arrival occurs around the azimuth of 215° which is also consistent with the observations.

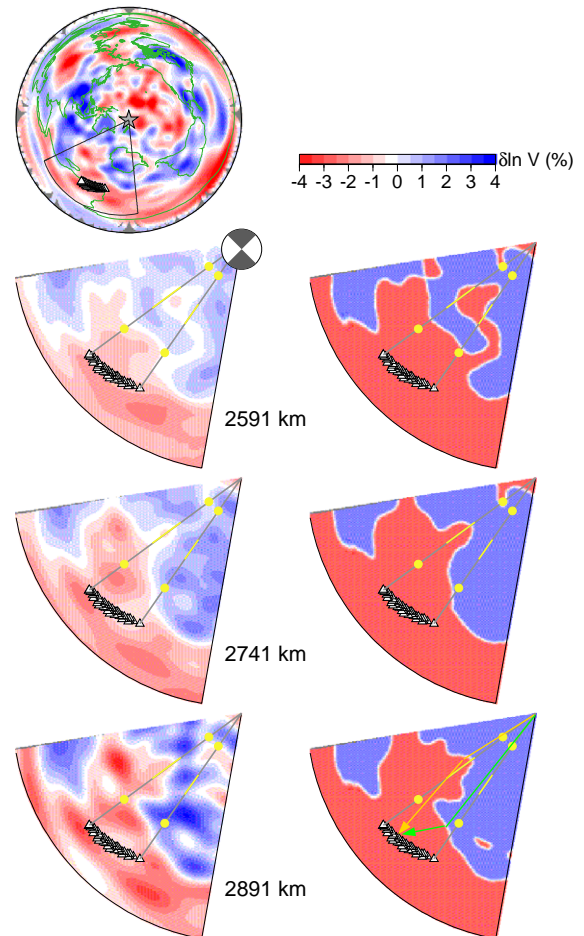


Fig. 10. Left panel: the original SAW24B16 model at three depths in the bottom 300 km of the mantle. The source in Fiji Tonga region is located at the apex. The stations in Africa (Fig. 1) are shown by triangles. Right panel: a model which is modified from SAW24B16. The boundary of the fast and slow anomaly is the contour line of 0 (%) anomaly of SAW24B16. The anomaly jump is from -2.75 to 1.75 (%). These values are determined by fitting travel time data. The model is expanded in spherical harmonics of up to degree 300, and the velocity jump of 4.5 (%) occurs within a distance of 100 km at the CMB. Both models have 1D PREM structure from surface down to 370 km above the CMB. The 3D velocity anomalies linearly increase from 370 to 300 km above the CMB.

Fig. 12(a) and (b) shows the synthetic and observed particle motions at the station corresponding to an azimuth of 210.26° . The particle motion of Sdiff phase in 1D PREM model (shown by a grey line) shows almost purely tangential motion at the azimuth of maximum SH radiation. The synthetic particle motion indicates that the first pulse arrives from the

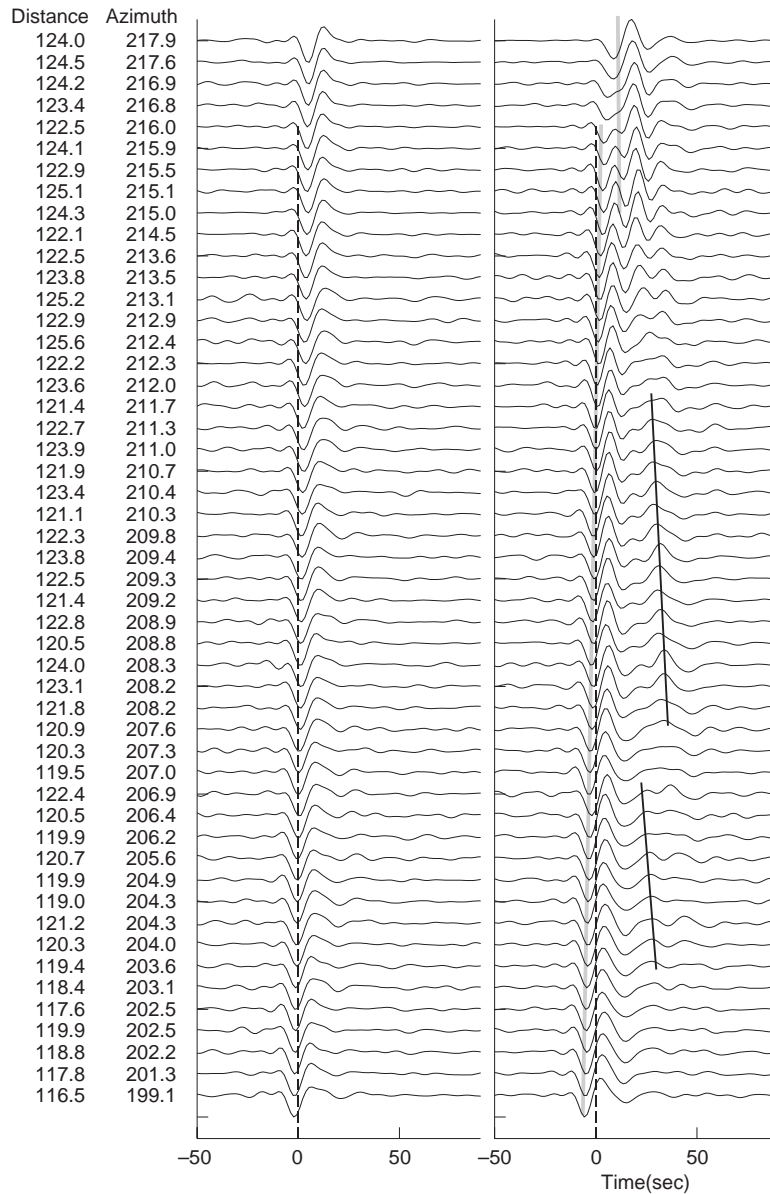


Fig. 11. Synthetic waveforms calculated by CSEM down to 8 s. (a) The waveforms from the original tomographic model (Fig. 10 left panel); (b) the waveforms from the modified model (Fig. 10 right panel). Gray lines follow the first trough, black lines follow the secondary arrivals.

southern side and the second pulse arrives from the northern side. Although the timing of the second arrival is not quite consistent, the observed particle motion also follows a similar trend. Both the first and second arrivals are estimated to be refracted waves and their paths are described schematically in Fig. 10 by yellow and green lines, respectively. We should

point out, however, that several observations show similar particle motion as Fig. 12(b), and many of the observed traces are complicated or do not show the clear change of the incoming wave direction (Fig. 12(c)(d)). The modified model is consistent with the result from the previous section, where Fig. 8(f) looked most similar to the data. In both Fig. 8(f) and

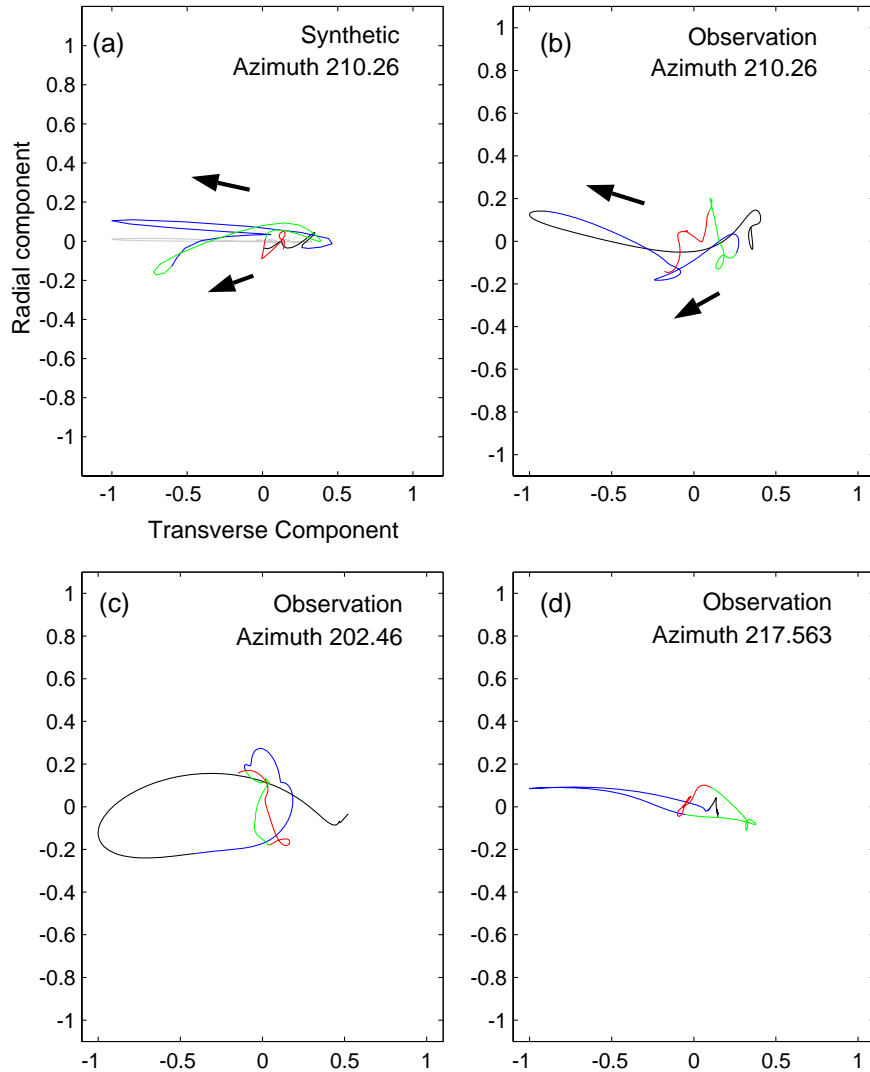


Fig. 12. Comparison between synthetic (a) and observed (b) particle motions at one of the stations of the African array. The station is located at an azimuth of 210.26° and a distance of 121.09° . The color indicates the time with respect to predicted Sdiff arrival from PREM. Black: -35 to -5 s, Blue: -5 to 20 s, Green 20 to 45 s, Red 45 to 70 s. Gray line shows the particle motion calculated from PREM. Arrows indicate the motion of the first and second pulse. (c) and (d) are also observed particle motions at the stations located at an azimuth of 202.46 and 217.563 respectively.

Fig. 11(b), the source is located on the faster side of the boundary, the velocity jump is 4% and 4.5% respectively, and the multiple pulses are observed at stations located on the slow side.

The particle motions depend also on radiation pattern and anisotropic structure. For example, particle motion plots show evidence for shear wave splitting (elliptical motion) for paths that stay entirely in the fast

region (azimuths 199 – 204°) (Fig. 11c), but remain linear once the paths start interacting with the vertical boundary and for the rest of the azimuth range considered here (Fig. 11d). This is consistent with the absence of prominent SV energy for azimuths larger than 204 (Fig. 2 second panel) and indicates that neither radial anisotropy, as found in many regions in D'' [27], nor azimuthal anisotropy can explain the secondary

pulses described in this study. We defer a detailed analysis of the full suite of observed particle motions to a future study.

5. Discussion and conclusion

The result from simple models (Figs. 7 and 8) shows that when the wavepath in D'' is quasi parallel to a sharp vertical boundary, the Sdiff waveforms are accompanied by secondary phases. The synthetic tests from the models of Fig. 7 give only a qualitative constraint on the model, which is the existence of a sharp vertical boundary in the D'' region. However, because SEM includes the 3D effects from strong heterogeneous structures, the order of magnitude of the effects on the waveforms is well captured by the simple model. When the boundary is sharper, the secondary phases are clearer and observed in wider ranges of azimuth. These phases can be used as additional constraints on the shape and sharpness of these boundaries. There are features in the synthetic waveforms of Fig. 8, which are not seen in observed waveforms. They are indicated by grey dots, and are observed at those receivers, where the wave paths only sample the slow anomaly regions and do not interfere with the lateral heterogeneity. Therefore, we think the pulses are due to the vertical velocity change in the synthetic model, which is the sudden reduction of velocity at 300 km above the CMB. Various vertical structures should be examined and adjusted more carefully in future studies.

The synthetics from the more realistic model of Fig. 9 indicates that the postcursors of ASA data are refractions from different sides of the kidney shaped boundary. This suggests that the details of the shape and anomaly contrast at the boundary can be obtained by fitting the timing of the emergence of the postcursor. Although there are some differences, the timing of the first arrival and the slope of the secondary arrival are consistent between synthetics and observations. This indicates that the shape of the anomaly is well described in the existing tomographic model, in spite of the fact that only 2D kernels within the great circle were used to make the original model [3]. The gradient of the anomaly is less well constrained, as previously discussed in the case of Africa by Ritesma et al. [5] and in the case of the Pacific by Breger and

Romanowicz [16]. Observation of refracted waves outside of the great circle suggests the importance of including 3D effects for detailed modeling of the velocity anomalies at the base of the mantle. These effects should also be examined carefully when attenuation measurements are made in regions with sharp lateral heterogeneity, or more generally, when modeling amplitudes of low pass filtered records.

The observed waveforms of ASA (Fig. 2) are presented in other papers [12,15]. Wen [12] proposed a model where the thickness and velocity of the low velocity region varies from a 12 km thick layer with -12% velocity reduction on the south side, to a 180 km thick layer with negative velocity gradient of -2% at the top and -9% at the CMB on the north side. The shape of the slow anomaly region in Wen's model is consistent with this study, however, his modeling requires a large velocity contrast. In his study, only 2D heterogeneity along the great circle was taken into account to construct the synthetic waveforms for the modeling. The postcursors were interpreted as reflections inside the low velocity layer on the CMB, in the vertical plane. In contrast, we interpret the secondary pulses as arising from interactions with the vertical boundary, in the horizontal plane. Since the D'' region is characterized by strong heterogeneity having a broad spectrum of scale lengths, it is important to identify whether the secondary pulses are caused by vertical or lateral heterogeneity. Different interpretations result in quite different models [28–30]. Our result is consistent with Ni et al. [15]. Here, we show that the observed multiple pulses can be produced from relatively simple structures. In addition to the pulses pointed out in Ni et al. [15] (shown by grey lines in Fig. 2), we show that the observed Sdiff phase is followed by a postcursor (shown by solid black lines in (Figs. 2, 3 and 8)), which can be explained by a strong vertical boundary. The emergence of pulses due to heterogeneity outside of the great circle are more consistent with the data than effects from horizontal layering. Furthermore, by considering 3D effects, we find that a relatively small velocity contrast across the vertical boundary (but stronger on average over the last 300 km of the mantle than in current tomographic models) is sufficient (about 4%). Breger and Romanowicz [16] obtained a large 8% lateral shear velocity gradient across the northeastern boundary of the

Pacific superplume, at the base of the mantle. Similar trends in differential travel time shifts as in Fig. 6 were measured in that study. Because, in that study, the velocity structure was modified only locally near the CMB, rather than changing the gradient and saturating a large region with constant anomaly, the velocity change may be consistent with what is found here.

We have shown that sharp vertical boundaries exist not only at the border of the African plume but also under the south Pacific. The Sdiff waveforms, which graze these two regions, are similar in that 1) rapid shifts of the first arrival time with respect to azimuth are observed; 2) secondary phases, which accompany the Sdiff phase (shown by solid black lines in Figs. 2 and 3) are observed; 3) smaller pulses are observed at higher frequencies, which can be followed in a certain azimuth range (shown by open circles in Figs. 2 and 3). This indicates that the low velocity regions in the lower mantle under Pacific and Africa, corresponding to the strong degree-2 pattern in shear velocity tomographic models, have a similar nature also at finer scales. The velocity contrast found here, averaging 4–4.5%, is smaller than suggested in some previous forward modeling studies, however, it is still significantly larger than in any recent S velocity tomographic models, which clearly underpredict lateral variations in the last 300 km at the base of the mantle (e.g. [5,31]).

Such a large average anomaly over this depth range cannot be due to thermal effects alone and implies that the superplumes carry a distinct compositional component. Unlike the African superplume where the shape and the location of much of the boundaries are revealed thanks to data from dense broadband arrays, large uncertainties remain on the shape of the Pacific superplume. In particular, the locations of northern and western boundaries of the Pacific superplume need to be further investigated, as well as finer scale structure within the superplumes.

Acknowledgments

The IRIS Data Management Center provided the wave forms used in this study.

We thank Vernon Cormier and two anonymous reviewers for useful comments, and Doug Dreger for

helpful discussions. This study was supported by a grant from NSF (EAR-0106000). Berkeley Seismological Laboratory Contribution #05-03.

References

- [1] S.P. Grand, Mantle shear-wave tomography and the fate of the subducted slabs, *Phil. Trans. R. Soc. Lond.* 360 (2002) 475–2491.
- [2] Y.J. Gu, A.M. Dziewonski, W.J. Su, G. Ekström, Models of the mantle shear velocity and discontinuities in the pattern of lateral heterogeneities, *J. Geophys. Res.* 106 (2001) 11169–11199.
- [3] C. Mégnin, B. Romanowicz, The three-dimensional shear velocity structure of the mantle from the inversion of body, surface and higher-mode waveforms, *Geophys. J. Int.* 143 (2000) 709–728.
- [4] G. Masters, G. Laske, H. Bolton, A.M. Dziewonski, The relative behavior of shear velocity, bulk sound speed, and compressional velocity in the mantle: implications for chemical and thermal structure, in: S. Karato, A. Forte, R. Liebermann, G. Masters, L. Stixrude (Eds.), *Earth's Deep Interior: Mineral Physics and Tomography from the Atomic to the Global Scale*, Geophysical Monograph 17, AGU, Washington, DC, 2000, pp. 63–87.
- [5] J. Ritsema, H.J. van Heijst, J.H. Woodhouse, Complex shear wave velocity structure imaged beneath Africa and Iceland, *Science* 286 (1999) 1925–1928.
- [6] S. Tanaka, Very low shear wave velocity at the base of the mantle under the South Pacific superswell, *Earth Planet. Sci. Lett.* 203 (2002) 879–893.
- [7] E.J. Gamero, D.V. Helmberger, Travel times of S and SKS: implications for three-dimensional lower mantle structure beneath the central Pacific, *J. Geophys. Res.* 98 (1993) 8225–8241.
- [8] M.E. Wysession, L. Bartko, J. Wilson, Mapping the lowermost mantle using core-reflected shear waves, *J. Geophys. Res.* 99 (1994) 13667–13684.
- [9] J. Ritsema, S. Ni, D.V. Helmberger, H.P. Crotwell, Evidence for strong shear velocity reductions and velocity gradients in the lower mantle beneath Africa, *Geophys. Res. Lett.* 25 (1998) 4245–4248.
- [10] M.E. Wysession, K.M. Fischer, G.I. Al-eqabi, P.J. Shore, I. Gurari, Using MOMA broadband array ScS–S data to image smaller scale structures at the base of the mantle, *Geophys. Res. Lett.* 28 (2001) 867–870.
- [11] L. Bréger, B. Romanowicz, C. Ng, The Pacific plume as seen by S, ScS, and SKS, *Geophys. Res. Lett.* 28 (2001) 1859–1862.
- [12] L. Wen, Seismic evidence for a rapidly varying compositional anomaly at the base of the Earth's mantle beneath the Indian Ocean, *Earth Planet. Sci. Lett.* 194 (2001) 83–95.
- [13] S. Ni, E. Tan, M. Gurnis, D.V. Helmberger, Sharp sides to the African super plume, *Science* 296 (2002) 1850–1852.
- [14] A.M. Dziewonski, D.L. Anderson, Preliminary reference Earth model, *Phys. Earth Planet. Inter.* 25 (1981) 297–356.

- [15] Sidao Ni, D.V. Helmberger, J. Tromp, 3D structure of the African super plume from waveform modeling, *Geophys. J. Int.* (in press).
- [16] L. Bréger, B. Romanowicz, Three-dimensional structure at the base of the mantle beneath the central Pacific, *Science* 282 (1998) 718–720.
- [17] B. Hager, R.W. Clayton, M.A. Richards, R.P. Comer, A.M. Dziewonski, Lower mantle heterogeneity, dynamic topography and the geoid, *Nature* 313 (1985) 541–545.
- [18] S.G. Robertson, J.H. Woodhouse, Ratio of relative S to P velocity heterogeneity in the lower mantle, *J. Geophys. Res.* 101 (1996) 20041–20052.
- [19] W.J. Su, A.M. Dziewonski, Simultaneous inversion for 3-D variations in shear and bulk velocity in the mantle, *Phys. Earth Planet. Inter.* 100 (1997) 135–156.
- [20] M. Ishii, J. Tromp, Normal-mode and free-air gravity constraints on lateral variations in velocity and density of the Earth's mantle, *Science* 285 (1999) 1231–1236.
- [21] G. Schubert, G. Masters, P. Olson, P. Tackley, Superplumes or plume clusters? *Phys. Earth Planet. Inter.* 146 (2004) 147–162.
- [22] Y. Capdeville, Méthode couplée éléments spectraux-solution modale pour la propagation d'ondes dans la Terre à l'échelle globale, Thèse, vol. 7, Université Paris, 2000.
- [23] Y. Capdeville, E. Chaljub, J.P. Vilotte, J.P. Montagner, Coupling the spectral element method with a modal solution for elastic wave propagation in global earth models, *Geophys. J. Int.* 152 (2002) 34–66.
- [24] Y. Capdeville, A. To, B. Romanowicz, Coupling spectral elements and modes in a spherical earth: an extension to the "sandwich" case, *Geophys. J. Int.* 154 (2003) 44–57.
- [25] A. To, Y. Capdeville, B. Romanowicz, Waveform modeling of 3D structure of D'' region using a coupled SEM/Normal Mode Approach, Fall '03 meeting abstract, *EOS Trans. A. G. U.*, 2003, S31D-0787.
- [26] B.L.N. Kennett, O. Gudmundsson, Ellipticity corrections for seismic phases, *Geophys. J. Int.* 127 (1996) 40–48.
- [27] M. Panning, B. Romanowicz, Inference on flow at the base of Earth's mantle based on seismic anisotropy, *Science* 303 (2004) 351–353.
- [28] X.F. Liu, J. Tromp, A.M. Dziewonski, Is there a first-order discontinuity in the lowermost mantle? *Earth Planet. Sci. Lett.* 160 (1998) 343–351.
- [29] V.F. Cormier, Some problems with S, SKS and ScS observations and implications for the structure of the base of the mantle and outer core, *J. Geophys.* 57 (1985) 14–22.
- [30] R.A.W. Haddon, G.G.R. Buchbinder, Wave propagation effects and the Earth's structure in the lower mantle, *Geophys. Res. Lett.* 13 (1986) 1489–1492.
- [31] L. Bréger, B. Romanowicz, L. Vinnik, Tests of tomographic models in D'' using differential travel times, *Geophys. Res. Lett.* 25 (1998) 5–8.